Friction **10**(4): 608–629 (2022)
https://doi.org/10.1007/s40544-021-0523-3
ISSN 2223-7690
CN 10-1237/TH
RESEARCH ARTICLE

Experimentally validated atomistic simulation of the effect of relevant grinding parameters on work piece topography, internal stresses, and microstructure

S. J. EDER[1,2,*], P. G. GRÜTZMACHER[2], T. SPENGER[3], H. HECKES[4], H. ROJACZ[1], A. NEVOSAD[1], F. HAAS[3]

[1] *AC2T research GmbH, Viktor-Kaplan-Straße 2/C, Wiener Neustadt 2700, Austria*

[2] *Institute of Engineering Design and Product Development, TU Wien, Lehárgasse 6—Objekt 7, Vienna 1060, Austria*

[3] *Institute of Production Engineering, Graz University of Technology, Kopernikusgasse 24/I, Graz 8010, Austria*

[4] *Tyrolit – Schleifmittelwerke Swarovski K.G., Swarovskistraße 33, Schwaz 6130, Austria*

Received: 11 December 2020 / Revised: 26 February 2021 / Accepted: 29 April 2021

Abstract: In this work, we present a fully atomistic approach to modeling a finishing process with the goal to shed light on aspects of work piece development on the microscopic scale, which are difficult or even impossible to observe in experiments, but highly relevant for the resulting material behavior. In a large-scale simulative parametric study, we varied four of the most relevant grinding parameters: The work piece material, the abrasive shape, the temperature, and the infeed depth. In order to validate our model, we compared the normalized surface roughness, the power spectral densities, the steady-state contact stresses, and the microstructure with proportionally scaled macroscopic experimental results. Although the grain sizes vary by a factor of more than 1,000 between experiment and simulation, the characteristic process parameters were reasonably reproduced, to some extent even allowing predictions of surface quality degradation due to tool wear. Using the experimentally validated model, we studied time-resolved stress profiles within the ferrite/steel work piece as well as maps of the microstructural changes occurring in the near-surface regions. We found that blunt abrasives combined with elevated temperatures have the greatest and most complex impact on near-surface microstructure and stresses, as multiple processes are in mutual competition here.

Keywords: large-scale molecular dynamics; surface quality; microstructure; Revolutions per minute-Synchronous Grinding (RPM-Synchronous Grinding); tool wear

1 Introduction

Machining processes like grinding are often the only mechanical finishing processing options able to meet the given precision requirements, which is why they are part of almost all manufacturing processes [1, 2]. The ongoing demand for highly efficient processes also drives the development of optimized grinding operations. In this context, the tool–work piece interaction largely determines the efficiency of the grinding process, the work piece quality, and the machining time [3]. By selecting the grinding parameters, the tool–work piece interaction and thus finally the efficiency of the process can be controlled [3]. An in-depth understanding of the influence of the combined set of grinding parameters on the resulting grinding process is necessary to be able to optimize the process. This is all the more important as the ground surface represents the final surface quality [2], thus highly influencing component functionality and longevity [4]. Despite grinding processes usually being optimized for surface quality and the geometric shape of the work piece, lately a materials science perspective has been added to the analysis, specifically focusing on the microstructural

* Corresponding author: S. J. EDER, E-mail: stefan.j.eder@tuwien.ac.at

state of the work piece, as this has a strong influence on the mechanical properties of the material [5–7]. Thereby, not only the initial microstructure of the work piece is decisive but also the evolution of the microstructure in the near-surface zones [8], which are subjected to significant stresses during the grinding process [9, 10]. Resulting from the modification of the mechanical properties in the near-surface zones, the efficiency of the grinding process or the durability of either tool or work piece might be considerably affected [11]. Pressure and heat are the grinding parameters that most critically affect the material properties of the work piece and the grinding process [12]. By increasing the pressure, grinding productivity may be increased, but this usually comes at the cost of a lower surface quality such as higher surface roughness or surface hardness [5, 13]. High temperatures, on the other hand, which might result from friction during the grinding process can lead to grain growth, softening of the near-surface zones, phase transformations, burning, and cracks [2, 12, 14, 15]. Moreover, variations in pressure and temperature also considerably affect chip morphology. Apart from the grinding parameters, the tool itself naturally influences the grinding process. However, during the grinding process the tool geometry is changed as the abrasive particles are worn down, resulting in changes to the tool–work piece interaction.

An important result of the factors mentioned above is visible in the form and shape of the resulting grinding chips. A well-working grinding process can often be defined by the shape of the chips [16]. There are all kinds of different shapes and sizes of chips, ranging from small drizzle to continuously formed strings of work piece material. There is one unifying concept behind all chip formation: A detachment of material has to be provoked by force, which usually forms alongside the primary deformation zone, also defined as a shear plane or shear zone, with a certain angle towards the machined work piece surface [6, 17]. This is defined by multiple process parameters, most importantly the involved geometries, the sharpness of the tool, which is also defined by the rake angle, the work piece material, cutting speed, infeed depth, and many more, which are also mutually interdependent [11, 18]. For example, the overall geometries of tool and work piece, the cuts per pass, and the infeed depth collectively determine the overall contact area of the process, which in turn will influence the chip thickness. On the other hand, the peripheral grinding speed will decrease the chip thickness and improve surface quality, but also increase the risk of thermal damage by an increase of temperature in the grinding zone [2], which can thus again reduce the surface quality. Furthermore, not every set of parameters will form a proper chip at all, because additional effects of deformation are involved. These effects are friction, furrowing, and plowing, which will all result in an increase of heat and pressure, but do not contribute to efficiently grinding the work piece. Although these effects can be useful in processes like shear spinning or spin forging, they are mostly regarded as negative or unwanted [17]. A process with insufficient chip generation will usually result in a high concentration of surface defects, burn marks, and microstructural changes [19].

In a more in-depth approach, these effects can even be scaled down onto a single grain analysis with closeups on the chip roots, involving mechanisms like micro-grooving or micro-flow-chipping [20]. Such analyses will highlight the importance of an ideal rake or separation angle in combination with a sharp enough grinding tool (down to a single grain) for the work piece material in question [6]. Therefore, many experiments have already been conducted to understand the systems behind chip formation, including geometrical influences like the undeformed chip thickness [17, 21], shearing, tip angles, and cutting velocities [22], and relating to these, the specific material removal rates of a system. Rather than being only a function of the abrasive grain size, the surface quality is strongly determined by their shapes and peak radii. However, the influences above are not the only sources defining chip formation [23]. Additionally, the work piece material itself significantly affects chip formation, as this is critically influenced by the material properties such as density, elasticity, hardness, or heat capacity [24]. To gain a sound understanding of the relation between grinding parameters and grinding process, a highly time- and space resolved investigation of the surface and the underlying microstructure is required. In this context, it has been shown for sliding events that microstructural changes can occur even after one single contact between counterbody and substrate [25].

Simulations have evolved far enough to aid the achievement of the topographic and near-surface microstructural qualities required by industry [26, 27], and now constitute a powerful means of optimizing processes while maintaining the mandated tolerances [3] for properties such as roughness or hardness. Progress in high performance computing has made molecular dynamics (MD) simulations and other meshless simulation methods a viable tool for studying the processes occurring during scratching [28], cutting [29], milling [30], or grinding [31]. Notable previous efforts of simulating scratching, cutting, or polishing atomistically have been dedicated to understanding exit-burr formation [32], the removal of a single nanoscale chip from a monocrystalline or amorphous flat surface [33] or from an isolated roughness feature [34, 35], and to studying some of the occurring crystallographic processes. Based on polycrystalline MD models featuring tens of millions of atoms, we can nowadays make predictions about the outcome of nanoscopic grinding and sliding processes that can be qualitatively translated to the micro scale because the simulated grains are sufficiently large to correctly reproduce a realistic material response [36]. Hence, MD simulations offer the possibility to understand the processes that take place during grinding in terms of microstructural evolution and surface quality, thus being a powerful tool to optimize such processes from the bottom up.

In this work we will introduce our atomistic approach to modeling a finishing process of polycrystalline ferrite/steel and give details on our choices of system layout, work piece microstructure, abrasive size, and process kinematics that facilitate a comparison with macroscopically ground surfaces. Then, a brief overview of the experimental test setup and procedure is given, including the subsequent surface measurement approach. First, we present the quantitative and qualitative topographic and force results obtained from the MD simulations. This data is subsequently validated and compared with the results from the macroscopic grinding tests either directly (in case of the steady-state normal force on the work piece) or via normalization by the abrasive size for the surface roughness. With our validated model, we then go on to study and discuss aspects of near-surface work piece development that are laborious to measure experimentally or even impossible to observe *in-situ*, namely stresses within the work piece and its microstructural evolution.

2 Modeling details

All MD simulations were carried out using the open source software LAMMPS [37]. The primary MD model, a ferrite work piece with a bimodal grain size distribution, was constructed in Dream.3D [38], see the upper part of Fig. 1, where all particle system visualizations were done in OVITO [39]. Both grain sizes were chosen to be equiaxed, with mean grain diameters of 28.3 nm and 14.2 nm, respectively. The initial 3D-periodic system of 85 nm × 85 nm × 85 nm then holds approximately 200 grains that are randomly oriented.

The Dream.3D microstructure was imported into Matlab, all grains filled with bcc lattices (a = 2.86 Å) oriented in the directions determined by Dream.3D, and then an atomically flat work piece surface was introduced by deleting all atoms with z > 40 nm, see Fig. S1 in the electronic supplementary material (ESM). After energy minimization and heat treatment by heating up to 1,100 K, followed by a cooling cycle down to 300 K, the grain boundaries were assumed to be in thermodynamic equilibrium, and a small amount of initial roughness is introduced by equilibration processes in the individual grains. The interactions within the ferrite work piece were governed by a Finnis–Sinclair potential with parameters from Ref. [40].

As a simple model for a "mild steel" work piece, we introduced a cementite (Fe_3C) phase, see the bottom panels in Fig. 1. This second MD model is identical to the ferrite in terms of size, grain structure and orientations, except that the smaller (14.2 nm) grains were filled with a cementite lattice as a second phase, leading to an overall carbon content of 2.66 wt%. For the steel work piece, we used a three-body Tersoff interaction potential with the parameters taken from Ref. [41].

The abrasives representing the grinding tool were constructed as alumina (α-Al_2O_3) particles. Three alumina parallelepipeds with Gaussian size distribution were prepared and placed with varying rake angles above the work piece surface as can be seen on the left side of Fig. 1, following a protocol that is described

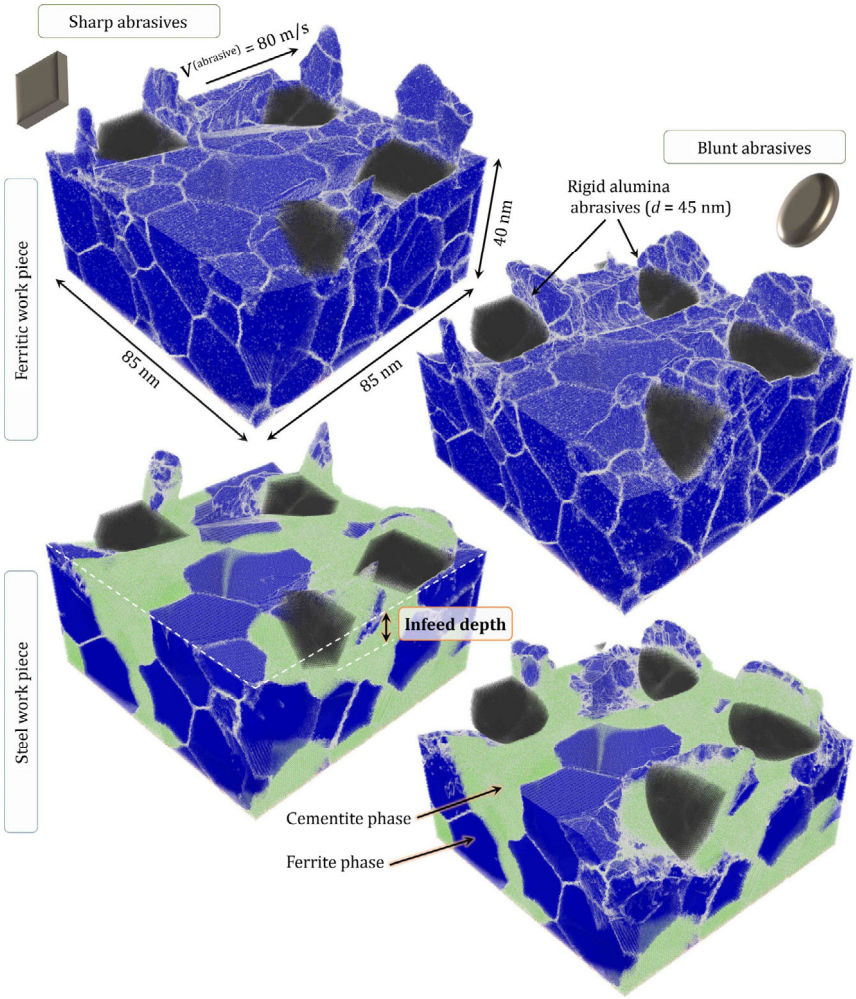

Fig. 1 MD work piece and system overview. Snapshots of four different configurations at the same time during grinding at 12 nm infeed depth. Top systems: ferritic work piece; bottom systems: steel work piece; left column: sharp abrasives; and right column: blunt abrasives. bcc Fe atoms are blue, grain boundaries white, C atoms green, so that the cementite phases look pale green. Abrasives are gray. The particle system visualizations were done in OVITO.

for generic abrasives in Ref. [42]. Both work pieces were fitted with 3 abrasives with a mean diameter of 45 nm, yielding an areal coverage fraction of 22%, which agrees well with typical bearing area fractions of freshly dressed industrial grinding tools (20%–30%) and also reflects a realistic ratio between the sizes of the abrasive grains and the grains in the work piece microstructure.

The arrangement, shape, and sizes of the modeled abrasives were quantitatively defined in advance to best resemble the configuration in a realistic grinding wheel. As a computational simplification, the grinding tool is assumed to be completely rigid, which is a common assumption in grinding simulations where the hardness between work piece and grinding tool differ significantly. The abrasives interact with the work piece via a Lennard–Jones potential, with σ = 2.203 Å calculated from interatomic first-neighbor distances using the Lorentz–Berthelot mixing rules, the energy parameter ε = 0.095 eV optimized via a parametric study to imply the existence of a medium [43], and a cutoff radius of 10 Å. Therefore, the abrasives behave like alumina in terms of crystallography and shape, but not strictly in terms of hardness and possible chemical interaction with the work piece.

To cover the two extremes of sharp and edgy as well as blunt and worn abrasives, we constructed systems where the three alumina abrasives cleft along crystallographic planes are replaced with ellipsoids of identical axis dimensions, see the right side of

Fig. 1. This, of course, comes at the expense of crystallographically well-defined abrasive surfaces, but the main intent here was to study the effect of a more conformal contact during grinding, with a higher fraction of plowing rather than cutting, thus mimicking worn abrasives. While the "atomically sharp" abrasive edge radii are smaller than 0.5 nm, the effective blunt edge radii vary about 14 ± 8 nm depending on the orientation of the abrasive with respect to the work piece surface. It should be noted that the simulated abrasive blunting cannot perfectly correspond to that in the real system, especially with respect to the abrasive grain morphology. However, in experimental investigations we do observe some flattening of the abrasives, leading to changes in the curve radii, more conformal contact, and subsequently more plowing than cutting, which are exactly the phenomena that we intended to capture in our model.

During the grinding simulations, periodic boundary conditions were applied in both lateral directions. Infeed depths of the abrasives into the work piece in $-z$ direction were varied between 5, 8, 10, and 12 nm, with the most data being available for the lowest and highest values. Simultaneously, the abrasives were moved at constant speed of v_x = 80 m/s and v_y = 9 m/s over the work piece, cutting chips of various lengths and shapes depending on the infeed depth and the simulation time. The velocity component in y direction was introduced to prevent the abrasives from immediately grinding in their own grind marks upon re-entering the periodic simulation box from the $-x$ direction, but rather meet up with the same portions of the work piece after approximately 10 passes. Thus, these kinematics correspond well to Revolutions per minute-Synchronous Grinding (RPM-Synchronous Grinding) processes [44, 45], where the same abrasives come into contact with the same work piece areas again and again in the course of machining, which means that the work piece surface can be influenced in a much more defined way compared to grinding with no defined speed ratio between work piece and grinding wheel. The time step was set to 2 fs, and a Langevin thermostat with a coupling time of 3.5 ps was applied in y direction to keep the temperature of the substrate at the desired value while reproducing a realistic heat conductivity of ferrous work pieces [46]. In order to obtain data for a range of temperatures that might occur directly at the interface between abrasive grain and work piece during the grinding process, we performed simulations at 300, 600, and 900 K, as maintaining the correct heat conductivity with a work piece thickness of 40 nm does not allow the surface to heat up by more than approximately 100 K [47]. The lowest 3 Å of the work piece were kept rigid to avoid torque on the work piece during grinding.

Grain refinement and defect formation were quantified via common neighbor analysis (CNA) [48]. Note that CNA itself cannot distinguish between grain boundaries, defects, and surfaces. The depth- and time-resolved evolution of the grain boundary and defect fractions was produced by space-averaging the quantity of interest over lateral layers with a thickness of 1 nm (corresponding to approximately 6×10^5 atoms).

The correct automatic identification of chips is the basis for calculating material removal as well as obtaining the time-resolved surface topography. Any atom that has moved in grinding direction faster than half of the grinding velocity was defined as part of a chip. Chip formation during grinding is a cumulative process, therefore the respective atom even remains part of the chip if its advection velocity should ever drop below this threshold velocity [49].

The surface roughness of the simulated work piece topographies was then quantified by its root-mean-square (RMS) value, equivalent to the S_q roughness parameter. In addition, the power spectral densities of simulated and experimentally obtained work piece topographies were calculated parallel and normal to the grinding direction according to Refs. [50, 51] for comparison purposes.

3 Experimental details

In the MD simulation method described above, the same abrasives repeatedly interact with the same work piece areas over the course of the process simulation due to the periodic boundary conditions. These process kinematics and conditions correspond closely to RPM-Synchronous Grinding, in which the speeds of work piece and grinding wheel are coupled in a defined ratio, so this process was selected to validate the simulation approach in terms of surface quality and microstructure development. The process particularity

of RPM-Synchronous Grinding can be exploited to influence the work piece surface in a highly defined manner and to produce a wide spectrum of non-circular geometries without an oscillating pendulum movement of the grinding wheel [45, 52].

The test setup, test procedure, relevant process parameters, as well as more detailed information regarding the work piece surface measurements are shown in Fig. 2 and Table 1 and described in the following two subsections.

3.1 Test setup and procedure

In order to represent realistic conditions for finishing applications in the experimental tests, grinding wheels with more than mesh 120 according to Federation of European Producers of Abrasives (FEPA) standard/ less than average grain size of 120 μm [18] and mild process parameter values in regard to a specific material removal rate Q'_w of 1.5 mm²/s or less [53] are recommended. To allow comparative tests with the MD simulations, conventional vitrified bonded grinding wheels with an average grain size of 58 μm are used.

The standard work piece material used to compare the achieved surface quality with the MD results in this study is the steel 1.3505 (DIN EN ISO 100Cr6/AISI SAE 5210) in the hardened state, as this material meets numerous requirements in the field of automotive engineering and is therefore used for camshafts or for rolling elements in bearings. The surface hardness is defined and measured at 57 HRC, the hardening depth at 1.3 mm. The pre-machined cylindrical work piece with an outer diameter of 54 mm and a length of 80 mm was designed so that two grinding areas are made available per work piece. As shown in Fig. 2 (bottom right), all work pieces are pre-ground before the actual grinding process, so that the oxide layer formed during hardening is removed and all work pieces have a comparable cylindricity. In the grinding process itself, material is then machined from all work pieces to just below the hardening depth, so that on the one hand representative material areas are always machined and on the other hand various intermediate states can be examined in terms of surface technology. In order to generate an appropriately sharp grain on the grinding wheel at the beginning of the test series, the wheel is freshly dressed by the rotating form roll. Subsequently, a large amount of work piece volume is removed without re-dressing the

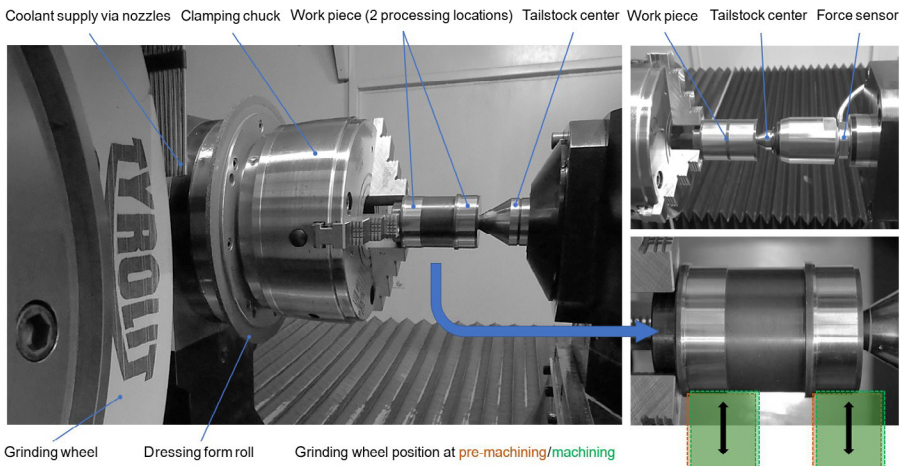

Fig. 2 Overview of performed experimental investigations. Left: general test set-up. Top right: test set-up force measurement. Bottom right: detail of ground work piece with two processing locations, grinding wheel positions shown schematically.

Table 1 Experimental process parameters (dressing and grinding).

Grinding wheel		Grinding parameter					Dressing parameter		
Specification	Grain size d_k (μm)	Circumferential speed V_g (m/s)	Speed ratio i_g	Relative velocity V_{rel} (m/s)	Specific material removal rate Q'_w (mm³/(mm·s))	Removed work piece volume V_w (mm³)	Overlap ratio U_d	Velocity ratio q_d	Depth of cut a_d (mm)
CS55A220II5VK1	58	50	–1	54.4	1.5	28,500 (2 × 2,850 each work piece)	80	–0.7	0.005
			+1	45.6					

grinding wheel, so that a realistic industrial grinding process including tool wear can be simulated, and a work piece surface that has been machined with a worn grinding wheel (corresponding to "blunt" abrasives) can be generated and examined.

As a suitable option for process monitoring, a sensor-equipped grinding tool can be selected to collect information about the general grinding process [54]. A piezoelectric 3-component force sensor (KISTLER type 9047C) is used to measure three orthogonal components of the resulting grinding force. To enable a force measurement as direct as possible in the force shunt, it is arranged on the tailstock—Fig. 2 (top right). Due to the high work piece speeds occurring in the process, a rotating center is required on the tailstock, otherwise overheating and deformation would occur due to the axial work piece clamping force and the resulting friction between tailstock tip and work piece. Since the sensor detects secondary forces (clamping, work piece weight, imbalance of the rotating work piece) in addition to the forces occurring during the actual grinding process, the sensor is calibrated with a spring scale in tangential and normal direction before the grinding process. The grinding forces determined by this force measurement can be evaluated and converted into a representative specific unit (N per mm grinding wheel width) and a contact pressure for comparison with simulation results.

3.2 Surface measurement

Optical and tactile surface measurements of the ground surfaces were carried out. For three-dimensional (3D) topography and 2D surface roughness parameters, the confocal microscopes LEICA DCM 3D and LEICA DCM8 with a 20× magnification objective lens were used. Two opposing scanning areas with 6 mm × 1.8 mm were defined for each cylindrical surface. For the additional tactile detection of the line roughness parameters, a HOMMEL ETAMIC W20 was used to examine five individual profiles along the circumference parallel to the work piece cylinder axis. Applicable DIN and ISO standards were observed for measurement and analysis of the confocal and the tactile approaches.

For the investigated grinding process, also called "Synchro-Finish" in the finishing community, the root-mean square (RMS) deviation ultimately proved to be best suitable for comparing the properties of the considered steel work piece topographies [55]. As mentioned earlier, the 2D topographic images also served as a data basis for calculating the averaged one-dimensional power spectral density, parallel as well as normal to the grinding direction, which was then compared to that obtained from the simulated work piece topographies.

3.3 Scanning electron microscope image

In addition to the hardened steel work pieces mentioned above, we also ground pure ferrite samples (ARMCO ® Pure Iron) with similar parameters as described in Section 3.1, but with a higher relative velocity of up to 68 m/s in order to best compare microstructural changes caused by the grinding process with the ferrite microstructure obtained from the MD simulations. After grinding of these soft ferrite samples, a longitudinal section was cut out with a lab scale cut-off machine DiscoTom 100 (Struers Corp., Denmark). Gentle cutting and optimized cooling were performed to prevent any changes to the material caused by cutting. Afterwards, a metallographic cross-section (longitudinal section with respect to the grinding direction) of the specimen was prepared via embedding, fine grinding, and polishing. A metallographic routine optimized for high resolution at the interface between work piece and embedding compound was used in the sample preparation. Scanning electron microscopy (SEM) and focused ion beam investigations were performed employing a Jeol JIB4700F cross-beam SEM (Jeol Ltd., Japan). Image was performed after ion etching for 3 s at 30 kV acceleration voltage and a beam current of 10 nA. Ion images were acquired with the secondary electron detector at 30 kV acceleration voltage and 30 pA probe current for optimal orientation contrasting. SEM images of the microstructure were taken at 15 kV acceleration voltage and a beam current of 1.2 nA. For best contrast between grains, the orientation-sensitive backscatter electron detector was chosen.

4 Results and discussion

4.1 Surface topography

Figure 3 gives an overview of the RMS roughness S_q

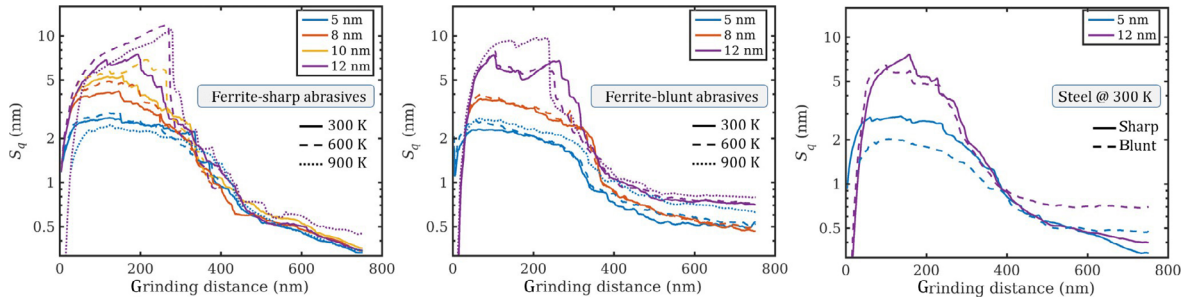

Fig. 3 Comparison of the time-resolved RMS roughness parameter S_q for all considered systems and several infeed depths (see legend). The grinding distance is the total length that the abrasive grains have moved along the work piece. Note the logarithmic scale in the vertical axes for ease of comparison of the optimum obtainable surface qualities.

obtained in the MD simulations as a function of the grinding distance (i.e., the total length that the abrasive grains have moved along the work piece). Since temperature and pressure are the two main parameters affecting the grinding process, the temperature and infeed depth (also controlling the pressure) were varied in the ranges 300–900 K and 5–12 nm, respectively. While it is clear that the highest of these temperatures would not be expected in a macroscopic finishing process, even highly localized temperature peaks near the cutting edges of the abrasives can have significant impact on the near-surface microstructure. Furthermore, the influence of wearing down the abrasive particles was simulated by considering sharp and blunt abrasives. Note that since the grinding tool is represented by three abrasive grains, each of which passes through the entire width of the simulation box approximately 9 times due to the periodic boundary conditions, every point on the work piece is machined by all three abrasives on average. As much more data is available for the ferrite work piece than for the steel work piece, the corresponding results were split into two graphs, one for new, sharp abrasives (left) and one for worn, blunt abrasives (center). All results for steel are shown in the right panel.

The time development of the surface roughness is shown on a logarithmic scale to better highlight the differences between the saturated values towards the end of the grinding process. Starting from an initial value close to zero, a result of the atomically flat initial surface, a typical curve for an infeed-depth-controlled grinding process is characterized by a steep increase in roughness as the abrasives cut into or plow through the work piece. This increase typically reaches a plateau after 50–100 nm of grinding distance, depending on the infeed depth, which also determines the height of the plateau (S_q roughly between 2 and 10 nm). The period from 0–300 nm of grinding distance is characterized by the largest topographic differences between the different infeed depths since up to roughly 300 nm the work piece is passed over only once by the abrasives, leaving more pronounced grinding marks in the surface at higher infeed depths. Between 300 and 400 nm of grinding distance, the roughness suddenly drops considerably as ridges that may have formed in the gaps between neighboring abrasives are abraded by other abrasives on a subsequent pass. This behavior seems to be more pronounced for larger infeed depths and higher temperatures. The former, because deeper grinding marks and more matter being moved allow the formation of steeper and higher ridges. The latter, because higher temperature makes the softer work piece more plastically deformable through dislocation mediated plasticity and subsequently leads to more plowing than cutting [7].

For the sharp abrasives, S_q is virtually independent of the infeed depth and the temperature after ~ 350 nm of grinding, and the surface quality increases at approximately the same rate for all process parameters. After 500 nm of grinding distance, this rate of quality improvement suddenly slows down for all processes with sharp abrasives, leading to a noticeable bend in the time development of S_q, which approximately marks the third pass of the entire set of three abrasives. At the end of the simulated grinding distance, almost all systems exhibit very low S_q values corresponding to only several monolayers of Fe atoms. The only system that ends up with an RMS surface roughness that is noticeably higher than in all other systems

is the one determined by the highest infeed depth (12 nm) and the highest temperature (900 K), where the deep grinding marks cannot be abraded anymore by subsequent passes of the abrasives.

For the worn, blunt abrasives, the behavior up to a grinding distance of 300 nm is similar to that of the sharp abrasives, but after the steep drop of the RMS roughness between 300 and 400 nm, S_q generally hovers at a higher level, and infeed depth as well as temperature related differences remain more pronounced. Here, the temperature dependence of the surface quality is most obvious for small infeed depth, where the highest temperature seems to limit the optimum achievable surface quality.

For the steel work piece, the above also seems to be valid, with the best achievable surface quality hardly distinguishable from that of the ferrite work piece. Thus, it can be stated that worn abrasives degrade the achievable surface quality of the ground work piece, which is more pronounced for high temperatures and infeed depths. By contrast, new and sharp abrasives lead to very high surface quality almost irrespective of the used infeed depth and temperature. Therefore, the geometry of the abrasives has a significant effect on the efficiency and quality of the grinding process, whereby the resulting roughness or surface quality also critically affects the friction and adhesion behavior [56], and thus the ongoing grinding process [57].

Figure 4 shows centered distributions of the final topographies after 3, 160, 320, 480, 640, and 750 nm of grinding distance at an infeed depth of 12 nm. For better comparability, all distributions were centered about their peak maxima. The insets represent the power spectral density normal to the grinding direction corresponding to the topographic distribution. High, narrow, and symmetrical peaks correspond to a smooth, high-quality surface whose peaks and valleys are evenly distributed. The lower and broader the peak, the rougher the surface, and the less the load bearing area is defined, see the top right panel in Fig. 4. Furthermore, the more asymmetrical the distribution, the more the surface is characterized by valleys below the load bearing area (in case of negative skew) or peaks above the load bearing area (positive skew). These graphs reform the data from Fig. 3 into a multi staged dynamic process analysis, which shows the transformation of the surface over time. One can identify different stages of the process, from deformation and chip formation to the resulting surface of the work piece, as shown later on in Fig. 5. This is immediately obvious when comparing t = 2 ns to t = 4 and 6 ns for sharp abrasives, where the peaks narrow down rapidly after the initial impact phase of the process, which is characterized by overall high roughness on both negative and positive sides. The sharp grains already produce a smoothly machined surface on the negative (valley) side after t = 4 ns, which will not further improve dramatically any more. At the same time there are still effects on the plus side of the graphs, introducing a strong positive skew that is evidence of peaks and ridges in form of not yet disconnected work piece material. Further continuation of the process will remove more material, smoothing the positive side of the graph and narrowing the peaks significantly, but the overall topography will remain rougher than that of the initial surface with a notably higher roughness on the peak-side, while the valley-side will be very close to ideal. This skewness effect is slightly shifted to the negative side for steel in comparison to ferrite, showing the characteristics of the work piece material.

From the distributions shown in Fig. 4, it can further be stated that temperature slightly reduces the height of the peak while somewhat broadening it, but it does not introduce any additional noticeable skewness to the topographic distribution. This is mostly true for both sharp and blunt abrasives, but when grinding with blunt abrasives, the overall topographic distribution changes significantly. In accordance with the evolution of S_q shown earlier, the peak maxima are typically lowered, representing a lower surface quality with higher roughness.

Furthermore, considerable negative skew is introduced. This skewness effect is more pronounced for the ferrite work piece than for steel, stronger at higher temperatures than at lower ones, and it also seems to be a slight function of the infeed depth (not shown). It results predominantly from the increased occurrence of the seemingly random topographic valleys (shown in blue in Fig. 5) that are promoted by the softening of the work piece as well as the plowing of the blunt abrasives. This also explains the stronger effect at higher temperatures, as deformation without chipping is more easily achieved on softer work piece

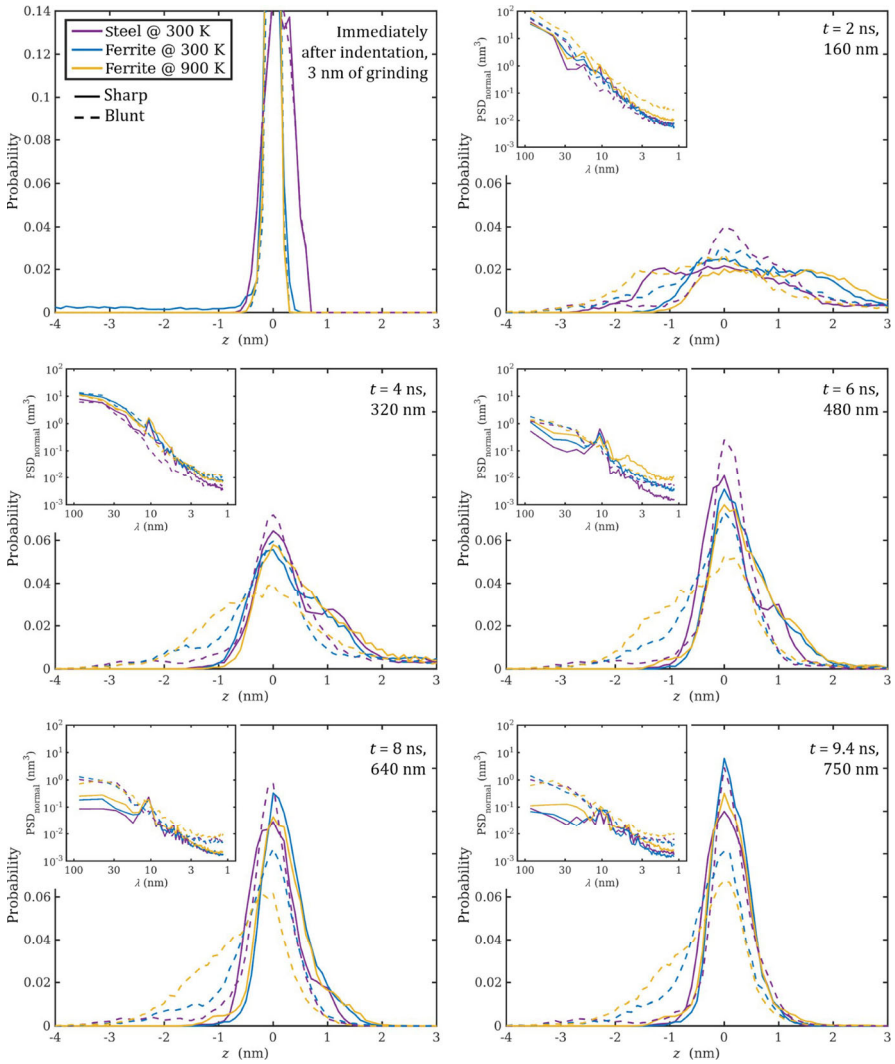

Fig. 4 Topographic distributions after 3, 160, 320, 480, 640, and 750 nm grinding distance at 12 nm infeed depth. All peaks have been centered about their maximum value, and the ordinate axis was scaled to show the most detail in the final configuration. Solid lines denote sharp abrasives, dashed ones blunt abrasives. A transposed version of this figure (one time series per panel) is available in Fig. S1 in ESM, along with an animation video of the entire time series. The insets show the power spectral density (PSD) of the topography at the specified time, averaged over 149 1D line scans normal to the grinding direction and plotted as a function of the wave length (note the logarithmic scales on both axes).

material. The deep impact indentation that occurs within the first 2 ns of grinding will not be smoothed out in the further process, which is in stark contrast to the improving surface behavior of sharp abrasives over time. This is especially important, as the positive roughness of the blunt abrasives is generally lower than that of the sharp abrasives, which however can yet be improved over time by additional abrasive passes, constituting a critical benefit.

A more exact feeling for the best achievable surface qualities can be obtained from comparing snapshots of the actual final topographies as shown in Fig. 5 for 5 and 12 nm infeed depth. Note that these topographies have been rotated so that the grinding grooves are horizontally aligned. For reference, the initial topographies as well as their respective topographic distributions and power spectral densities can be found in Fig. S2 in ESM. At 5 nm infeed depth and sharp abrasives, it seems that compared to the load bearing area, the grinding grooves seem to be slightly but consistently deeper and broader at 900 K. This again can be traced back to the higher plasticity of the material at higher temperatures, resulting in a higher amount of material moved by a single abrasive. At the

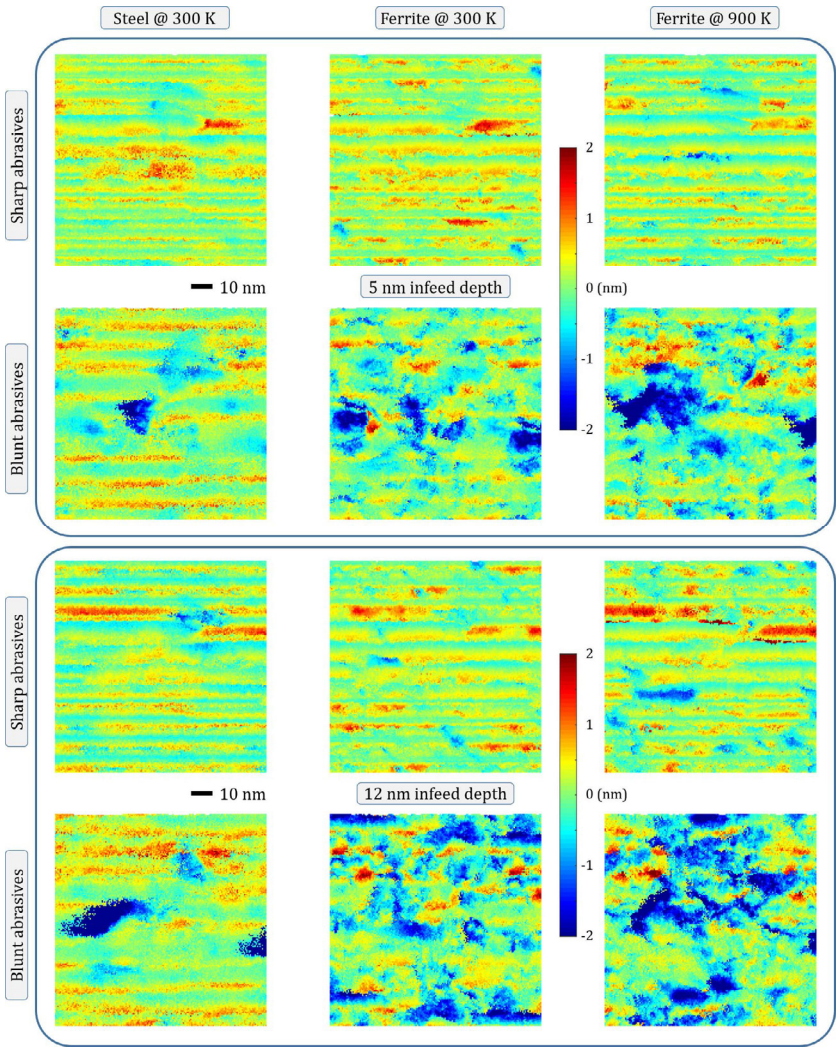

Fig. 5 Final simulated work piece topographies (height of surface z-coordinate) after a grinding distance of 750 nm at an infeed depth of 5 nm (upper box) and 12 nm (lower box). The color range is identical for all panels and has been centered about the peak of the topographic distribution. Left: steel at 300 K; center: ferrite at 300 K; and right: ferrite at 900 K. In each box, we compare final topographies produced by sharp (top row) and blunt abrasives (bottom row).

highest infeed depth of 12 nm and sharp abrasives, we observe an increased number of broader ridge peaks that remain on the final surface, while we also see a number of valley features that hardly exhibit any directionality in grinding direction, but rather seem to occur somewhat randomly. In particular, the ferrite work piece at 12 nm and 900 K exhibits a considerable amount of high and low points, which corresponds well to the overall higher roughness for that system in Fig. 3. In addition, this work piece seems to have some propensity towards the formation of very thin, but exposed burrs (see the upper third of the image).

Significant qualitative differences can be seen once the work pieces are ground using the blunt abrasives. It seems obvious that the topographies must be a result of an increased amount of plowing rather than clean cutting. Instead of continuous grinding grooves, we observe chopped and lumpy surface features that, for the ferrite work piece, hardly allow the recognition of the grinding direction from the topography. Due to its higher hardness, the steel work piece still exhibits grinding grooves, but these are much less distinct than those produced by the sharp abrasives. What is perhaps most obvious is the occurrence of seemingly random distributions of valley features (blue), preferably for the ferrite work piece at higher temperatures and at greater infeed depth. These features may be promoted by higher ductility due to increased

temperature, as well as the high normal pressures required to indent the blunt abrasives to greater depths into the work piece, leading to higher stresses in the latter. As can be seen from the topographic images, the blunt abrasives do not only result in a decrease of the surface quality by raising the surface roughness, but also by introducing asymmetry and an inhomogeneous distribution of roughness features with deeper valleys. Such surface features reduce the load bearing capacity and weaken the surface integrity of the ground work piece. This may result in higher friction and increase the risk of generating wear particles and high wear in general.

4.2 Validation by comparison with experiment

To validate our atomistic simulation approach qualitatively as well as quantitatively, we compare the MD simulation results in terms of topography and RMS roughness directly with those of our macroscopic grinding experiments that lead to RMS roughness values on the sub-micrometer scale. Figures 6(a) and 6(b) show representative surface topographies of work pieces ground with fine abrasive grain size (58 μm), once with a nearly freshly dressed grinding wheel after having machined only 2,850 mm³ (Fig. 6(a), "sharp"), which is equivalent to 15 fictitious work pieces, and once after having machined 28,500 mm³ (Fig. 6(b), "blunt"). As usual in industrial grinding processes, the temperature in the machining zone is kept as low as possible in order to avoid thermal damage to the work piece. For this reason, a sufficient amount of cooling lubricant is fed into the grinding gap by means of needle nozzles during the experimental tests (Fig. 2, left). Due to the relatively low temperature in the grinding gap and the fact that steel work pieces are ground, the images in Figs. 6(a) and 6(b) can best be compared with those in the left column of Fig. 5.

While it is clear that the final surface qualities between the two approaches lie approximately 3 orders of magnitude apart, this is also true of the abrasive sizes, namely 45 nm for the MD simulations and 58 μm for the macroscopic grinding tool. Considering some connection between the employed abrasive size and the resulting roughness reasonable and assuming linear scaling of roughness in a first approximation, we therefore normalize the best achievable surface quality in terms of S_q for the MD simulations and R_q for the grinding experiments with the respective abrasive grain size to yield a non-dimensional quantity. Even without the definite knowledge of a roughness scaling relation, we can thus achieve a qualitative comparison of surface roughness obtained with new/sharp abrasives to those obtained with worn/blunt abrasives, see Fig. 6(c), where we have averaged approximately 10

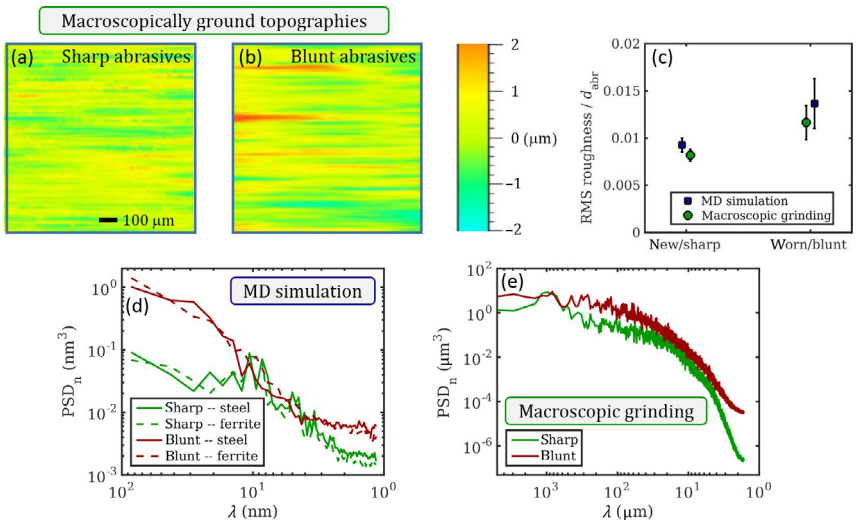

Fig. 6 On the validation approach: Final experimental surface topographies after grinding a work piece volume of 2,850 mm^3 (new grinding wheel—"sharp" abrasives, (a)) and 28,500 mm^3 (worn grinding wheel—"blunt" abrasives, (b)) in the macroscopic grinding test rig. (c) shows a comparison of the RMS surface roughness normalized by the mean abrasive diameter d_{abr} for the MD simulations and the macroscopic grinding experiments. (d) and (e) compare representative power spectral densities recorded from the final work piece topographies normal to the grinding direction for simulations (nm-scale) and experiments (μm-scale).

roughness values obtained in experiment and simulation with sharp and blunt abrasives for every plotted data point. R_q has the advantage of being quickly obtainable using a simple tactile analysis, while S_q provides much better statistics from the smaller set of simulated topography data, and since S_q is the 2D version of R_q, they are intrinsically comparable as long as the latter is measured normal to the grinding direction. While the model abrasives constitute the two extremes of sharpness and bluntness by construction, the real grinding tool was allowed to wear in operation as described above, which usually leads to flattened abrasive tips in the worn tool. The placement of the data points in the figure takes this qualitative difference into account by offsetting the MD results slightly towards the sides of the graph, which has the added advantage that the error bars are better visible. It is quite remarkable that not only the corresponding data points are quite close, but also the rate of surface quality deterioration with tool wear comes out almost identical. Although the abscissa in Fig. 6(c) is not a physical quantity but rather compares categories, the experimental data from Ref. [55] that would populate the region between the two extremes follows a nearly linear trend.

As both S_q and R_q are only scalar quantities that contain no information about the lateral distribution of roughness features or anisotropy, we also made a comparison between the power spectral densities recorded normally to the grinding direction (PSD_n) for the simulated and the macroscopically ground work piece topographies, see Figs. 6(d) and 6(e), respectively. Note that the abscissa shows the wave length of the roughness features, but with a reversed axis, so that the plot retains the usual feeling of having a frequency/wavevector as the argument. It should also be mentioned that the qualitative differences between Figs. 6(d) and 6(e) are amplified by the differences in the size of the underlying data sets (6,000 × 1,500 pixels for the experimental results, but only 149 × 149 for the computational ones). Although it is clear that the lateral topographic features differ by three orders of magnitude between simulation and experiment, there are several qualitative similarities between these plots. The RMS roughness is a function of the integral of PSD_n along the frequency axis, so an increase in roughness corresponds to a larger area encompassed by the corresponding curve. While this may seem trivial, the way in which the S-shaped PSD curves are pushed upwards by the blunting of the abrasives is similar between Figs. 6(d) and 6(e). The nature and quality of the ground surfaces seems from Figs. 6(d) and 6(e) as well as Figs. S3 and S4 in ESM to be random, but not self-affine, meaning that the Hurst exponent linked to fractal surfaces should not enter into the scaling. This, however, still does not yield a tangible scaling relation for roughness and abrasive size, so our linear assumption discussed above must remain a crude approximation. A certain wavelength range exists, centered around 20% of the abrasive size in both cases (5–10 nm for simulations and 5–20 μm for experiments), where the blunting of the abrasives has almost no effect on the final topography, whereas the contributions to the topography above and below this range amounts to between half and two orders of magnitude. The overlapping portions of the curves most likely stem from the similarity of the real contact area between sharp and blunt abrasives in this wavelength range, resulting in roughness features of similar size. The differences between the green and red curves in Fig. 6(d) for small wavelengths (~ 1–4 nm) are most likely caused by the strongly refined grains as well as the jagged edges of the plowing ridges in the wake of the blunt abrasives. By contrast, the difference between the two curves at greater wavelengths (~ 15–100 nm) is most probably due to the difference between the cutting edge radii of the abrasives. Finally, the anisotropy in the topography caused by the grinding marks has a similar quality between experiment and simulation, which can be seen in Figs. S3 and S4 in ESM.

Figure 7 gives an overview of the forces on the simulated work piece, both normal to the work piece surface and in cutting direction, normalized by the lateral system cross-section, yielding values that have the dimension of a pressure or a stress. We differentiate between the initial stresses that occur during the first stages of grinding and the steady-state stresses that can be expected to last until the process ends. The transition between the initial and the steady-state stresses (not shown) seems to proceed in two stages, with a steep decline of both normal and shear stress components within the first 150 nm of grinding, while the saturation to the steady-state values requires

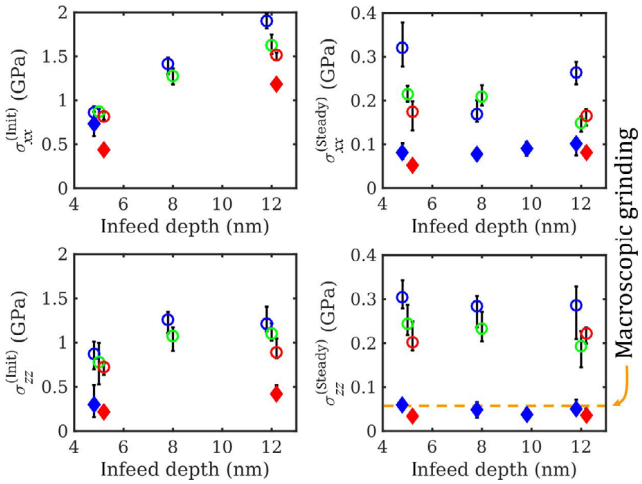

Fig. 7 Initial (left) and steady-state (right) cutting stresses (top) and normal pressures (bottom) on the ferrite work piece during the grinding simulations. The values and error bars represent medians and standard deviations over the initial and final 70 nm of grinding distance. Symbol colors denote different temperatures: 300 K—blue, 600 K—green, and 900 K—red. Diamonds denote sharp abrasives and circles denote blunt abrasives. The dashed horizontal line represents the steady-state normal pressure measured for a macroscopic grinding process with a freshly dressed grinding wheel.

approximately 500 nm of grinding. In the first stages, the first contacts between work piece and tool occur, and the abrasives are basically still being indented into the work piece, leading to high stresses of up to 2 GPa for the highest infeed depth of 12 nm. Afterwards, the stresses relax to their steady-state values between 0.05 and 0.35 GPa depending on the condition of the abrasive particles, the temperature, and the infeed depth. The first stages of grinding are associated with the running-in of the system, which is also reflected by the significant changes of the surface roughness S_q up to 500 nm of grinding, recall Fig. 3. In general, it can be said that depending on the infeed depth, the normal pressures and the cutting stresses relax to the range of 7%–35% of the initial value. From an energy efficiency perspective it seems most relevant to compare the steady-state stresses, as these are at play for extended periods of time. Here it can be stated that the energy requirements for grinding a given work piece with sharp or blunt abrasives (with otherwise identical process parameters) differ by a factor of almost 5, regardless of the considered stress component. It can be observed that the effect of temperature is minor for sharp abrasives but more pronounced for blunt abrasives.

For an infeed depth of 5 nm, for example, the cutting stresses at 900 K are only about half as high as at 300 K, which is a result of significant softening of metals at homologous temperatures above 0.4 T_m. In the bottom right panel of Fig. 7, we have added a dashed orange line representing the steady-state normal pressure of our macroscale grinding process (approximately 60 MPa) with a freshly dressed grinding wheel, thus being best comparable to the sharp abrasives (diamond symbols) in the simulation. Although values for σ_{zz} seem to be virtually independent of the infeed depth for a run-in grinding process, it is still remarkable how well they coincide with their macroscopic counterpart.

A comparison of the microstructural changes caused by grinding both experimentally and in the MD simulation is displayed in Fig. 8. As example for the initial and undisturbed microstructure of the ferritic sample, a representative area of the bulk material is displayed in Fig. 8(a), next to a cross-section of the

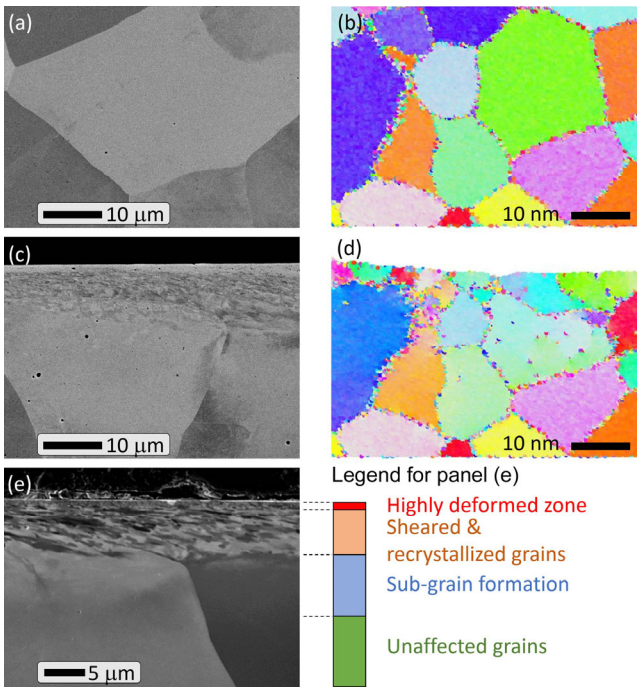

Fig. 8 Comparing SEM micrographs of a macroscopically ground ferrite work piece (a, c, e) with MD simulation results ((b, d): ferrite work piece at 300 K, 12 nm infeed) colored according to grain orientation (electron backscatter diffraction-Inverse pole figure (EBSD-IPF) standard). (a, b) Initial microstructure; (c, d) after grinding, with grain refinement. (f) Ion imaging close-up of experimental cross-section with annotations according to the observed deformation zones.

initial microstructure of the ferrite from MD simulation in Fig. 8(b).

The grain sizes can be estimated as 20–40 μm for the experimental sample, and they are 15–30 nm in the simulation model. This means a ratio between grain sizes of about 1,300, which is almost identical to the ratio between abrasive particle sizes of 58 μm and 45 nm. The microstructure after grinding the experimental sample is displayed as a SEM image and an ion imaging close-up of the experimental cross-section, with annotations according to the observed changes in microstructure in Figs. 8(c) and 8(e). For the simulated grinding process, the microstructure is shown as an EBSD-IPF image after the first pass of abrasive particles in Fig. 8(d). The simulated microstructure shows that the grains in the lowest 20 nm remain nearly unaffected, whereas changes in crystallographic orientation and the formation of sub-grains can be seen closer to the surface. In the topmost layer of the MD microstructure smaller, newly formed grains can be found. The microstructural processes observed after the experiment (in Figs. 8(c) and 8(e)) are qualitatively similar. The outermost 1 μm exhibits a highly deformed microstructure, with nearly no observable grains or boundaries. In the 5 μm below, we observe grains that were sheared in grinding direction (from right to left), where grain refinement and dynamic recrystallization are the dominating processes. Below that zone, sub-grain formation in the large ferritic grains can be seen, where the increased dislocation density at the grain boundaries leads to contrasting around the grain boundaries in both SEM and ion images. Further than 15–20 μm from the surface, no deformation process can be identified based on the acquired images. To gain a deeper insight into the ongoing deformation processes, the authors are currently carrying out further analyses, including EBSD measurements, which are suitable for describing structural material changes in tribologically affected zones to elucidate deformation with inverse pole figures (shearing) and misorientation plots, representing the local degree of deformation [58, 59].

4.3 Stresses and microstructural development in the work piece

Now that we can consider our simulation approach validated according to what was discussed above, we can take a time- and depth-resolved look at processes occurring within the work piece during grinding that are usually not readily observable *in situ*. We first discuss the distribution of stresses in grinding direction within the work piece. In Fig. 9, we have visualized the stress component σ_{xx} for all grinding processes at 12 nm infeed depth in the form of a heat map as a function of grinding distance and work piece depth. The differences between the ferrite and the steel work pieces can be summarized as the stress being higher, but more localized near the surface of the harder steel work piece. Due to increased softening of the work piece with rising temperature, the stress extends deeper into the work piece, which is particularly obvious during the indentation period at high temperatures. Again, the largest differences occur between grinding processes with sharp and blunt abrasives. Since the contact area between abrasive and work piece is larger for blunt abrasives, much higher forces are required to obtain the same infeed depth as with sharp abrasives.

This leads to higher stresses within the work piece, both in terms of the maximum absolute value (more

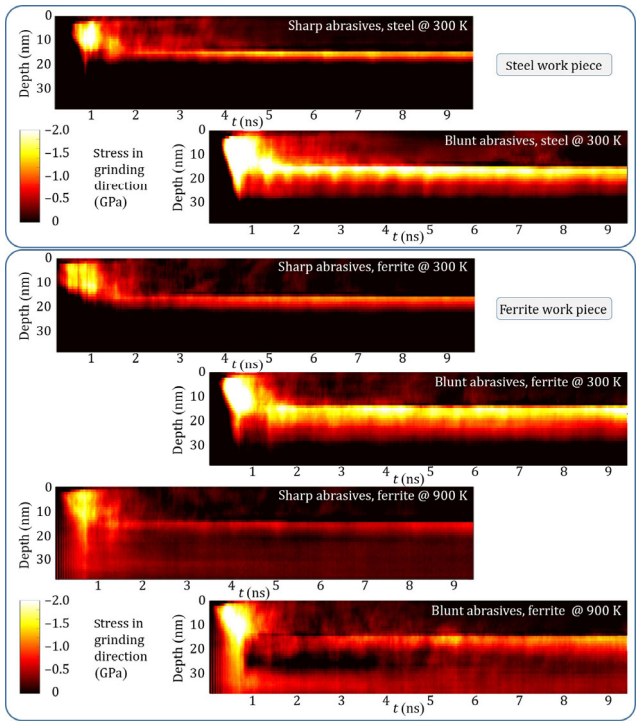

Fig. 9 Time- and depth-resolved maps of the stress in grinding direction at a constant infeed depth of 12 nm. The left column shows data for sharp, the right one for blunt abrasives.

than 2 GPa for blunt abrasives vs. 1.2–1.5 GPa for sharp ones) and the depth to which the stress extends. Especially the images for blunt abrasives at 300 K show that the stresses reach a depth of 25 nm below the original surface within the first nanosecond and remain at this depth for the remainder of the grinding process. This indicates significant plastic deformation and work hardening in the first grinding pass and no further hardening in the following passes. Again, the main difference between ferrite and steel lies in the stronger localization of the stress near the surface in the steel work piece. One noteworthy aspect of stress localization occurs only at high temperatures and predominantly when using blunt abrasives: in the ferrite work piece at 900 K we observe the establishment of a certain work piece depth (~ 25 nm) where the stress in grinding direction is considerably lower than in the neighboring layers. This can be attributed to relaxation and re-crystallization processes due to temperature and the amount of deformation. In general, the greater maximum stresses as well as the higher depth to which the stress extends at higher temperature and especially when grinding with blunt abrasives, may facilitate a greater degree of microstructural changes below the work piece surface, which will affect its mechanical properties and the response to ongoing loading [60]. Therefore, in a next step, we investigate the microstructure (quantified here as the grain boundary and defect fraction) in the near-surface region of the ground work pieces.

Figure 10 gives an overview of the grain boundary and defect fraction of the ferrite work pieces as heat maps depending on grinding distance and work piece depth for grinding processes with an infeed depth of 12 nm. Note that 4 out of the 6 panels are directly comparable to those in Fig. 9, but as our analysis approach does not allow us to produce this type of map for the steel work pieces, the resulting gap was filled with data for ferrite at 600 K, giving a better-resolved picture of the influence of temperature on the microstructure. We observe that for all systems, irrespective of the geometry of the abrasives and the temperature, the maximum in grain boundary and defect fraction occurs at around 1 ns of grinding as a response to the high stresses generated immediately before (Fig. 9).

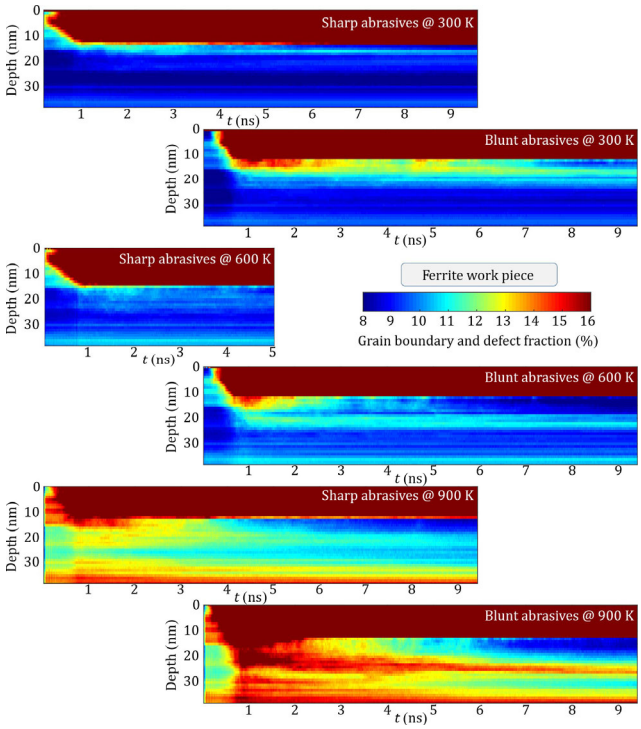

Fig. 10 Time- and depth-resolved maps of the grain boundary and defect fraction at a constant infeed depth of 12 nm at temperatures of 300 K (top), 600 K (center), and 900 K (bottom). The left column shows data for sharp and the right one for blunt abrasives. For sharp abrasives at 600 K, data is only available until t = 5 ns due to expiry of computational resources, and because microstructural effects emerge most clearly with blunt abrasives and at higher temperatures.

At this time of the grinding process, the highest density of defects is located in a region directly below the abraded surface. However, for the blunt abrasives and with increasing temperature, the grain boundary and defect fraction extends further into the work piece material, which is in accordance with the stress distributions in the corresponding systems as the stresses are the driver for these microstructural changes. With sharp abrasives and at low temperatures, only few lasting microstructural changes to the work piece seem to occur. The higher defect fraction close to the surface consists of dislocations, which are emitted as a result of the mechanical loading, and grain boundaries of small grains, which are either formed by partial abrasion of initially larger grains or as new grains by partial rotation of a grain and formation of a new grain boundary. This region of higher defect density is then either abraded in the course of grinding, or defects the deeper within the work piece

are reduced by recovery. Additionally, some dislocations rearrange and form new grain boundaries, which are also displayed as residual defects at a depth of around 5 nm below the new work piece surface.

However, if the abrasives wear down and become blunt, the grain boundary and defect fraction increases and extends further into the material. As the blunt abrasives cause higher stresses, which are also distributed over a wider region, there are also more instances of lattice rotation, more emitted dislocations, and greater amounts of newly formed grains. Therefore, this layer, characterized by an increased number of grain boundaries and intragranular defects, may constitute evidence for near-surface hardening. Similarly to the case of the sharp abrasives, this defect-rich surface layer is then partially abraded and slowly heals out by recovery during grinding. Due to the much greater number of induced defects and grain boundaries, however, there remains a considerable amount of residual defects in the material at the end of the simulated grinding process.

At 900 K, and particularly for the blunt abrasives, the defect fraction is at its maximum and extends into the work piece as far as the lower work piece border, which is in accordance with the higher stresses occurring in these systems. Additionally, the defect-rich layers are not abraded as quickly, since the more plastically deformable material is not directly abraded but rather plowed into high ridges. Despite the reduction of defects by the onset of recrystallization at 900 K and the sped-up recovery process at higher temperatures, via the promotion of diffusion, there are still many defects in the work piece at the end of the simulation as the temperature effect cannot fully compensate for the high defect fraction. The residual defects in the system with the blunt abrasives are mainly composed of newly formed grain boundaries by partial rotation of the initial grains and dislocation movement. By contrast, at 600 K the temperature-enhanced recovery results in a lower defect fraction at the end of the simulation compared to the system at 300 K. When comparing the panel with the results for blunt abrasives at 900 K with the corresponding stress map in Fig. 9, it can be seen that the work piece depth characterized by reduced stresses also has a higher density of defects. This means at this depth the stresses are consumed by the formation of defects and new grain boundaries, which then results in a distinctly localized layer over the course of the grinding process. In terms of the microstructural evolution it should be noted that a greater amount of defects and grain boundaries as well as a further extent of these defects into the surface does not necessarily constitute a disadvantage, as these microstructural changes can also improve surface properties with respect to their frictional or wear behavior [61, 62].

5 Conclusions

In this work we have performed a large-scale molecular dynamics parameter study of a grinding process with polycrystalline work pieces where we varied the work piece material (ferrite vs. carbon steel), the abrasive shape (sharp-edged vs. blunt), the infeed depth, and the temperature. The grain size was chosen large enough so that the microstructural response of the work piece to machining features several deformation mechanisms associated with macroscopic work pieces, although grain boundary processes that dominate the plasticity of nanoscopic grain structures are inevitably still present, which may be mitigated in future modeling efforts with larger grains. The periodicity of the work piece model, which is required to keep boundary effects from dominating the simulation results, together with the grinding kinematics that involve grinding at a slight angle to the simulation box, make our results best comparable to RPM-Synchronous Grinding, where similar portions of tool and work piece come into repeated contact with each other.

In order to justify our approach and in an attempt to validate the simulation results, such a grinding process was performed experimentally with sharp and worn grinding tools, and the obtained surface topographies were compared qualitatively and quantitatively. A comparison of the final work piece topographies showed that the computational results for the ferrite and the steel work pieces were nearly indistinguishable when ground with sharp abrasives, and these surfaces were in fair qualitative agreement with experimental topographies obtained with freshly dressed grinding wheels. This fact was seen as an

indication that the computationally less complex ferrite work piece can be used as a basis for comparison to the experimentally produced surfaces. As the ground work piece roughness obtained in the simulations lies almost exactly three orders of magnitude below the experimentally obtained one, the RMS roughness values were linearly normalized by the respective abrasive grain size. For want of a better approximation, this was done in the absence of the knowledge of a roughness scaling relation, the investigation of which constitutes an important topic of necessary future research. We found that not only did this roughness-to-abrasive-size ratio coincide between model and experiment, but also that the rate at which the surface quality deteriorates with a worn grinding tool (represented by the blunt abrasives in the simulation) was well reproduced. Reasonable qualitative agreement between simulation and experiments could also be shown for the power spectral densities of surfaces ground with sharp and blunt abrasives, as well as for the microstructural development of a pure ferrite work piece. In addition, the steady-state normal pressure at the end of the grinding simulations with sharp abrasives came out nearly identical to the 60 MPa measured in a grinding experiment with a freshly dressed grinding tool.

This good correlation between model and experiment motivated a more in-depth investigation of those aspects of grinding in the near-surface region of the work piece that are difficult or even impossible to observe experimentally. We studied the stresses in grinding direction as well as the grain boundary and defect fraction (a quantity that gives valuable clues about the microstructural development) within the work piece in a time- and depth-resolved manner. According to these visualizations, the cutting stresses in steel are more localized at the surface than in ferrite. In ferrite, blunt abrasives and higher grinding temperatures cause stresses to extend deeper into the work piece. A combination of blunt abrasives and high temperature led to the formation of a layer with reduced stresses, which was found to be characterized by a high density of defects and refined grains. Near the surface, initial work piece hardening was followed by subsequent annealing which was much more strongly pronounced at high temperatures.

The knowledge about the microstructural and residual stress development of a work piece as it undergoes its final production process should soon allow process engineers to tweak parameters in such a way that they obtain desired work piece properties while preventing unwanted effects such as thermal damage to the work piece (burning). Thus, simulations such as these may soon constitute an important tool in a two-way approach to process optimization. In the future, similar processes such as honing and Reishauer gear grinding may also be promising candidates for finishing methods that can be modeled and optimized using atomistic simulations.

Acknowledgements

This work was funded by the Austrian Research Promotion Agency FFG (Project SyFi, No. 864790). Part of this work was funded by the Austrian COMET-Program (Project K2 InTribology1, No. 872176) and carried out at the "Excellence Centre of Tribology". The computational results presented have been achieved using the Vienna Scientific Cluster (VSC). The government of Lower Austria is gratefully acknowledged for financially supporting the endowed professorship tribology at the Vienna University of Technology (Grant No. WST3-F-5031370/001-2017) in collaboration with AC2T research GmbH. The authors wish to thank Katharina Newrkla and Ulrike Cihak-Bayr for performing topography measurements of the experimental work pieces and providing pre-processed data for the PSD evaluations. Open access funding was provided by Vienna University of Technology (TU Wien).

Electronic Supplementary Material: Supplementary material is available in the online version of this article at https://doi.org/10.1007/s40544-021-0523-3.

References

[1] Arrazola P J, Özel T, Umbrello D, Davies M, Jawahir I S. Recent advances in modelling of metal machining processes. *CIRP Annals* **62**(2): 695–718 (2013)

[2] Malkin S, Guo C S. *Grinding Technology: Theory and Application of Machining with Abrasives*. New York (USA): Industrial Press Inc., 2008.

[3] Brinksmeier E, Aurich J C, Govekar E, Heinzel C, Hoffmeister H-W, Klocke F, Peters J, Rentsch R, Stephenson D J, Uhlmann E, et al. Advances in modeling and simulation of grinding processes. *CIRP Ann-Manuf Techn* **55**(2): 667–696 (2006)

[4] Wegener K, Bleicher F, Krajnik P, Hoffmeister H-W, Brecher C. Recent developments in grinding machines. *CIRP Annals* **66**(2): 779–802 (2017)

[5] Grützmacher P G, Gachot C, Eder S J. Visualization of microstructural mechanisms in nanocrystalline ferrite during grinding. *Mater Design* **195**: 109053 (2020)

[6] Swaminathan S, Shankar M R, Lee S, Hwang J, King A H, Kezar R F, Rao B C, Brown T L, Chandrasekar S, Compton W D, et al. Large strain deformation and ultra-fine grained materials by machining. *Mater Sci Eng A* **410**: 358–363 (2005)

[7] Beckmann N, Romero P A, Linsler D, Dienwiebel M, Stolz U, Moseler M, Gumbsch P. Origins of folding instabilities on polycrystalline metal surfaces. *Phys Rev Appl* **2**: 064004 (2014)

[8] Akcan S, Shah W S, Moylan S P, Chandrasekar S, Chhabra P N, Yang H T. Formation of white layers in steels by machining and their characteristics. *Metall Mater Trans A* **33**(4): 1245–1254 (2002)

[9] Jawahir I S, Brinksmeier E, M'saoubi R, Aspinwall D K, Outeiro J C, Meyer D, Umbrello D, Jayal A D. Surface integrity in material removal processes: Recent advances. *CIRP Annals* **60**(2): 603–626 (2011)

[10] Grützmacher P G, Rammacher S, Rathmann D, Motz C, Mücklich F, Suarez S. Interplay between microstructural evolution and tribo-chemistry during dry sliding of metals. *Friction* **7**(6): 637–650 (2019).

[11] Denkena B, Tönshoff H K. *Spanen: Grundlagen*. Heidelberg (Germany): Springer-Verlag, 2011.

[12] Malkin S, Guo C H. Thermal analysis of grinding. *CIRP Annals* **56**(2): 760–782 (2007)

[13] Zhou K, Ding H H, Wang W J, Wang R X, Guo J, Liu Q Y. Influence of grinding pressure on removal behaviours of rail material. *Trib Int* **134**: 417–426 (2019)

[14] Hwang J, Kompella S, Chandrasekar S, Farris T N. Measurement of temperature field in surface grinding using infra-red (IR) imaging system. *J Trib* **125**(2): 377–383 (2003)

[15] Moulik P N, Yang H T, Chandrasekar S. Simulation of thermal stresses due to grinding. *Int J Mech Sci* **43**(3): 831–851 (2001)

[16] Chen X, Schneider R, Gumbsch P, Greiner C. Microstructure evolution and deformation mechanisms during high rate and cryogenic sliding of copper. *Acta Mater* **161**: 138–149 (2018)

[17] Guo Y, Saldana C, Compton W D, Chandrasekar S. Controlling deformation and microstructure on machined surfaces. *Acta Mater* **59**(11): 4538–4547 (2011)

[18] Klocke F. *Fertigungsverfahren 2: Zerspanung mit geometrisch unbestimmter Schneide*. Berlin (Germany): Springer-Verlag, 2018.

[19] Holtermann R, Schumann S, Menzel A, Biermann D. Modelling, simulation and experimental investigation of chip formation in internal traverse grinding. *Production Engineering* **7**(2–3): 251–263 (2013)

[20] Denkena B, Köhler J, Kästner J. Chip formation in grinding: An experimental study. *Production Engineering* **6**(2): 107–115 (2012)

[21] Dai C W, Ding W F, Xu J H, Fu Y C, Tian Y. Influence of grain wear on material removal behavior during grinding nickel-based superalloy with a single diamond grain. *Int J Mach Tool Manu* **113**: 49–58 (2017)

[22] He C L, Zong W J, Zhang J J. Influencing factors and theoretical modeling methods of surface roughness in turning process: State-of-the-art. *Int J Mach Tool Manu* **129**: 15–26 (2018)

[23] Zitt U R. Modellierung und Simulation von Hochleistungsschleifprozessen. Ph.D. Thesis. Kaiserslautern (Germany): Kaiserslautern University, 1999.

[24] Steffens K. *Thermomechanik des Schleifens*. Düsseldorf (Germany): VDI-Verlag, 1983.

[25] Jacobs T D B, Greiner C, Wahl K J, Carpick R W. Insights into tribology from *in situ* nanoscale experiments. *MRS Bulletin* **44**(6): 478–486 (2019)

[26] Hashimoto F, Yamaguchi H, Krajnik P, Wegener K, Chaudhari R, Hoffmeister H-W, Kuster F. Abrasive fine-finishing technology. *CIRP Annals* **65**(2): 597–620 (2016)

[27] Khorasani A M, Yazdi M R S, Safizadeh M S. Analysis of machining parameters effects on surface roughness: A review. *Int J Compu Mater Sci Sur E* **5**(1): 68–84 (2012)

[28] Varga M, LerochS, Eder S J, Ripoll M R. Meshless microscale simulation of wear mechanisms in scratch testing. *Wear* **376**: 1122–1129 (2017)

[29] Goel S, Luo X C, Agrawal A, Reuben R. L. Diamond machining of silicon: A review of advances in molecular dynamics simulation. *Int J Mach Tool Manu* **88**: 131–164 (2015)

[30] Leroch S, Eder S J, Ganzenmüller G, Murillo L J S, Ripoll M R. Development and validation of a meshless 3d material point method for simulating the micro-milling process. *J Mater Process Tech* **262**: 449–458 (2018)

[31] Markopoulos A P, Karkalos N E, Papazoglou E-L. Meshless methods for the simulation of machining and micro-machining: A review. *Arch Comput Method E* **27**(3): 831–853 (2020)

[32] Fang F Z, Wu H, Liu Y C. Modelling and experimental investigation on nanometric cutting of monocrystalline silicon. *Int J Mach Tool Manu* **45**(15): 1681–1686 (2005)

[33] Pei Q X, Lu C, Lee H P, Zhang Y W. Study of materials deformation in nanometric cutting by large-scale molecular dynamics simulations. *Nanoscale Res Lett* **4**(5): 444–451 (2009)

[34] Agrawal P M, Raff L M, Bukkapatnam S, Komanduri R. Molecular dynamics investigations on polishing of a silicon wafer with a diamond abrasive. *Appl Phys A* **100**(1): 89–104 (2010)

[35] Zhong J, Shakiba R, Adams J B. Molecular dynamics simulation of severe adhesive wear on a rough aluminum substrate. *J Phys D Appl Phys* **46**(5): 055307 (2013)

[36] Eder S J, Ripoll M R, Cihak-Bayr U, Dini D, Gachot C. Unraveling and mapping the mechanisms for near-surface microstructure evolution in CuNi alloys under sliding. *ACS Appl Mater Inter* **12**(28): 32197–32208 (2020)

[37] Plimpton S J. Fast parallel algorithms for short-range molecular dynamics. *J Comput Phys* **117**: 1–19 (1995)

[38] Groeber M A, Jackson M A. Dream.3d: A digital representation environment for the analysis of microstructure in 3D. *Integr Mater Manuf I* **3**(1): 5 (2014)

[39] Stukowski A, Albe K. Extracting dislocations and non-dislocation crystal defects from atomistic simulation data. *Model Simul Mater Sc* **18**(8): 085001 (2010)

[40] Mendelev M I, Han S, Srolovitz D J, Ackland G J, Sun D Y, Asta M. Development of new interatomic potentials appropriate for crystalline and liquid iron. *Philos Mag* **83**: 3977–3994 (2003)

[41] Henriksson K O E, Nordlund K. Simulations of cementite: An analytical potential for the Fe–C system. *Phys Rev B* **79**(14): 144107 (2009)

[42] Eder S J, Bianchi D, Cihak-Bayr U, Gkagkas K. Methods for atomistic abrasion simulations of laterally periodic polycrystalline substrates with fractal surfaces. *Comput Phys Commun* **212**: 100–112 (2017)

[43] Eder S J, Cihak-Bayr U, Gachot C, Ripoll M R. Interfacial microstructure evolution due to strain path changes in sliding contacts. *ACS Appl Mater Inter* **10**(28): 24288–24301 (2018)

[44] Steffan M, Haas F, Spenger T. RPM-Synchronous Grinding: Control concepts to improve surface qualities for a highly efficient non-circular grinding approach. In *ASME 2017 International Mechanical Engineering Congress and Exposition*, Tampa, Florida, USA, 2017: V002T02A009.

[45] Spenger T, Haas F, Cihak-Bayr U, Eder S J, Weiß M, Weinzerl M, Schneider M. RPM-Synchronous Grinding—Investigation and comparison of surface topography of synchro-finish manufactured workpieces. *Procedia CIRP* **81**: 476–481 (2019)

[46] Eder S J, Cihak-Bayr U, Bianchi D. Large-scale molecular dynamics simulations of nanomachining. In *Advanced Machining Processes: Innovative Modeling Techniques*. Markopoulos A P, Davim J P, Eds. Boca Raton: CRC Press, 2018: 141–178.

[47] Eder S J, Grützmacher P G, Ripoll M R, Dini D, Gachot C. Effect of temperature on the deformation behavior of copper nickel alloys under sliding. *Materials* **14**(1): 60 (2021)

[48] Tsuzuki H, Branicio P S, Rino J P. Structural characterization of deformed crystals by analysis of common atomic neighborhood. *Comput Phys Commun* **177**(6): 518–523 (2007)

[49] Eder S J, Leroch S, Grützmacher P G, Spenger T, Heckes H. A multiscale simulation approach to grinding ferrous surfaces for process optimization. *Int J Mech Sci* **194**: 106186 (2021)

[50] Persson B N J, Albohr O, Tartaglino U, Volokitin A I, Tosatti E. On the nature of surface roughness with application to contact mechanics, sealing, rubber friction and adhesion. *J Phys-Condens Mat* **17**(1): R1 (2004)

[51] Jacobs T D B, Junge T, Pastewka L. Quantitative characterization of surface topography using spectral analysis. *Surf Topogr-Metrol* **5**(1): 013001 (2017)

[52] Spenger T, Haas F, Pichler J, Eder S J, Weinzerl M, Weiß M. RPM-Synchronous Grinding—An innovative and efficient manufacturing method for the production of non-circular workpieces. In *Proceedings of the ASME 2020 International Mechanical Engineering Congress and Exposition*, Portland, USA, 2020: IMECE2020–23859.

[53] Lierse T. Schleif- und Abrichttechnik. München (Germany): Carl Hanser Verlag, 2020.
[54] Brinksmeier E, Meyer L. Schleifprozessüberwachung mit sensorbestückten Werkzeugen. In *Autonome Produktion*. Klocke F, Pritschow G, Eds. Berlin, Heidelberg: Springer, 2004: 79–89.
[55] Newrkla K, Spenger T, Cihak-Bayr U. Systematic selection and evaluation of relevant surface roughness parameters for the characterisation of the innovative RPM-Synchronous Grinding process. *Surf Topogr-Metrol* **9**: 015022 (2021)
[56] Milanese E, Brink T, Aghababaei R, Molinari J-F. Emergence of self-affine surfaces during adhesive wear. *Nat Commun* **10**(1): 1116 (2019)
[57] Hinkle A R, Nöhring W G, Leute R, Junge T, Pastewka L. The emergence of small-scale self-affine surface roughness from deformation. *Sci Adv* **6**(7): eaax0847 (2020)
[58] Rojacz H, Mozdzen G, Weigel F, Varga M. Microstructural changes and strain hardening effects in abrasive contacts at different relative velocities and temperatures. *Mater Charact* **118**: 370–381 (2016)
[59] Schwartz A J, Kumar M, Adams B L, Field D P. *Electron backscatter diffraction in materials science*. New York (USA): Springer, 2009.
[60] Argibay N, Furnish T A, Boyce B L, Clark B G, Chandross M. Stress-dependent grain size evolution of nanocrystalline Ni–W and its impact on friction behavior. *Scr Mater* **123**: 26–29 (2016)
[61] Argibay N, Chandross M, Cheng S F, Michael J R. Linking microstructural evolution and macroscale friction behavior in metals. *J Mater Sci* **52**(5): 2780–2799 (2017)
[62] Prasad S V, Michael J R, Battaile C C, Majumdar B S, Kotula P G. Tribology of single crystal nickel: Interplay of crystallography, microstructural evolution, and friction. *Wear* **458–459**: 203320 (2020)

S. J. EDER. He received his Ph.D. degree in technical physics in 2012 for the atomistic simulation of mixed- and boundary-lubricated friction contacts. Since 2007, he has been working at Excellence Centre of Tribology (AC2T research GmbH), first as a project manager and now also as principal scientist. In 2015, he received a research grant to simulate abrasive processes occurring during polishing and grinding at multiple length scales. Since 2018, he is also active as a research associate in Carsten Gachot's tribology group at Vienna University of Technology (TU Wien). His research interests include near-surface microstructural development of polycrystalline metals in sliding contacts and in finishing processes.

P. G. GRÜTZMACHER. He received his Ph.D. degree in materials science in 2019 from Saarland University under the guidance of Frank Mücklich (Institute of Functional Materials) for the tribological investigation of multi-scale surface textures. Since 2019, he works in Carsten Gachot's tribology group at TU Wien as postdoctoral researcher. His current research interests focus on near-surface microstructural development of polycrystalline metals during sliding, tribological mechanisms of 2D materials, and surface engineering.

T. SPENGER. He obtained bachelor and master degrees at Graz University of Technology with a specialization in production science and automotive engineering. He has several years of practical experience as a project engineer in the automotive testing industry. Since 2017, he is enrolled in the doctoral program in mechanical engineering as a university assistant at Graz University of Technology with a specialization in grinding technology.

H. HECKES. He studied mineralogy at RWTH Aachen University. He started working at Saint-Gobain Abrasives in 2006 as a researcher on the functionality of vitrified grinding wheels. This was also the topic of his diploma thesis in 2008, focusing on the resulting system strength of different glass matrices based on external influences. He continued working in this area of expertise at Tyrolit Schleifmittelwerke Swarovski K.G. as product developer and group leader for vitrified conventional tools. He specializes in the analysis of chemical and physical interactions between bond matrix and grain.

H. ROJACZ. He is a senior scientist at Austrian Centre of Competence for Tribology. His educational background is materials science as well as energy- and environmental science. He has more than ten years' experience in materials tribology and materials analysis techniques such as scanning electron microscopy (SEM) and electron backscatter diffraction (EBSD). His research is mainly focused on high-temperature wear, wear-resistant coatings, and microstructural changes in tribological contacts.

A. NEVOSAD. He received his Ph.D. degree in materials science in 2013 from Montanuniversität Leoben for conductive probe based investigations on ZnO varistor ceramics. Since 2014, he is employed at AC2T research GmbH, first as project manager in the field of wear reduction and since 2020 as leader of the research area "friction optimized devices". His research activities comprise wear and friction phenomena on various materials like metals, polymers, and coatings in various load conditions and environments.

F. HAAS. He studied mechanical engineering and economics and received his Ph.D. degree from Graz University of Technology in 1996. Afterwards he was managing director in the family-owned mechanical engineering company. From 1997 on, he also taught at University of Applied Sciences Campus 02, where he worked as a mechanical engineering professor from 2007 to 2013. He was appointed head of the Institute for Production Engineering at TU Graz in 2013. Since 2020, he holds the position of the faculty dean of mechanical engineering and economic sciences at Graz University of Technology.